Check for updates

Sustainable and energy-saving hydrogen production *via* binder-free and *in situ* electrodeposited Ni–Mn–S nanowires on Ni–Cu 3-D substrates†

Ghasem Barati Darband, [ID] *[a] Danial Iravani, [ID] [b] Meiling Zhang, [ID] [c] Meysam Maleki, [ID] [d,h] Shanrui Huang,[c] Seyyed Mehdi Khoshfetrat, [ID] [e] Reza Andaveh[f] and Jinyang Li [ID] *[c,g]

Electrochemical water splitting, with its oxygen evolution reaction (OER) and hydrogen evolution reaction (HER), is undoubtedly the most eco-friendly and sustainable method to produce hydrogen. However, water splitting still requires improvement due to the high energy consumption caused by the slow kinetics and large thermodynamic potential requirements of OER. Urea–water electrolysis has become increasingly appealing compared to water-splitting because of the remarkable decline in the cell potential in the hydrogen production process and less energy consumption; it also offers a favorable opportunity to efficiently treat wastewater containing a significant amount of urea. In this work, Ni–Mn–S/Ni–Cu nano–micro array electrocatalysts were synthesized by a two-step and binder-free electrochemical deposition technique and investigated as an effective electrode for the HER and urea oxidation reaction (UOR). According to the electrochemical results, the optimized electrode (Ni–Mn–S/Ni–Cu/10) showed excellent electrocatalytic activity for the HER (64 mV overpotential to achieve the current density of 10 mA cm^{-2} and Tafel slope of 81 mV dec^{-1}) in alkaline solution. When Ni–Mn–S/Ni–Cu/10 is employed as a UOR anode in an alkaline solution containing urea, it achieves a current density of 10 mA cm^{-2} at 1.247 V *vs.* RHE. In addition, when the optimized sample was utilized as a bi-functional electrode for overall urea–water electrolysis (HER-UOR), the cell voltage reached 1.302 V at 10 mA cm^{-2} (which is 141 mV less than that for HER-OER). The electrocatalytic stability results unequivocally revealed small changes in voltage during a 24 h test and showed good durability. This non-noble metal electrocatalyst, prepared by the electrodeposition synthesis method, is a promising solution to implement low-cost hydrogen production and wastewater treatment.

[a] Materials and Metallurgical Engineering Department, Faculty of Engineering, Ferdowsi University of Mashhad, Mashhad 91775-1111, Iran. E-mail: baratidarband@um.ac.ir
[b] Chemical Engineering Department, Faculty of Engineering, Ferdowsi University of Mashhad, Mashhad, Iran
[c] School of Chemistry, Key Laboratory of Advanced Technologies of Materials (Ministry of Education), Southwest Jiaotong University, Chengdu 610031, China. E-mail: jinyang.li@swjtu.edu.cn
[d] Department of Chemical and Materials Engineering, Concordia University, Montreal, Quebec H4B 1R6, Canada
[e] Department of Chemistry, Faculty of Basic Science, Ayatollah Boroujerdi University, Borujerd, Iran
[f] Department of Mechanical and Materials Engineering, University of Western Ontario, London, Ontario, N6A 5B9 Canada
[g] Yibin Institute of Southwest Jiaotong University, Yibin 644000, China
[h] Department of Materials Engineering, Faculty of Engineering, Tarbiat Modares University, P.O. Box: 14115-143, Tehran, Iran
†Electronic supplementary information (ESI) available. See DOI: https://doi.org/10.1039/d4nr03486d

1. Introduction

Due to its remarkable efficiency (an energy density of approximately 120 MJ kg^{-1}), abundance, and eco-friendliness, hydrogen (H$_2$) is considered to be the greenest and most promising energy carrier.[1,2] Electrochemical water electrolysis into oxygen and hydrogen is a green and sustainable approach to harvest hydrogen energy.[3–5] Generally, water electrolysis comprises two half-reactions: HER and OER. The OER entails a stage of multi-proton-coupled electron transfer, which exhibits slow kinetics and remains a crucial aspect in the overall water electrolysis (OWS) procedure.[6,7] To avoid this bottleneck and realize efficient electrochemical hydrogen generation, it has been suggested to substitute water molecules with other readily oxidized ingredients. So far, hydrazine, urea, and methanol have been explored as replacements for water molecules to make electrochemical hydrogen generation more

energy-efficient.[8–10] The electro-oxidation of urea is generally employed in the treatment of urea-rich wastewater while simultaneously acquiring high-purity hydrogen.[7,11,12] By using UOR instead of OER, there will be a 36% cost savings from a hydrogen production efficiency perspective.[7] In comparison to the thermodynamics cell voltage of 1.23 V required for water electrolysis, the overall cell voltage for urea electrolysis is 0.37 V under standard conditions. Urea has the advantages of being non-toxic, low-cost, and easy to transport in comparison with hydrazine and methanol. Furthermore, it is one of the most widely used nitrogen fertilizers and an important chemical intermediate;[13] besides, urea-rich wastewater is produced daily in large quantities.[14,15] Human urine contains a concentration of 0.1 to 0.5 M urea, which is its major organic component.[16] As a result, urea can be considered as a major source for hydrogen production. Though the electrochemical method is favorable for urea elimination, the initial reaction kinetics of urea oxidation is relatively slow due to a six-electron transfer procedure on the anode.[17,18] As a result, high-efficiency electrocatalysts need to be developed to perform urea oxidation reaction.

Similar to HER and OER, UOR uses precious metal-based electrocatalysts (Pt, Ru, and Pd).[19] Still, the shortage and high cost of these materials have hindered their widespread application on an industrial scale and the commercialization of technologies based on urea.[20,21] Ni-based catalysts are among the most reported metallic catalysts due to their promising performances in the urea oxidation reaction.[22–24] The production cost, difficult experimental conditions, and low conductivity of nickel metal are typical problems associated with nickel-based electrocatalysts. These factors can hinder electronic transmission between interfaces and boost energy consumption,[25,26] thus failing with respect to the long-term stability.[27–29] Alloying nickel with other active metal elements is one of the methods that can improve the catalytic activity.[30,31] Copper is a highly conductive element that can be alloyed with nickel to obtain superior performance in HER and OER. This is due to the favorable adsorption energy of H* and OOH, which enables the alloy to exhibit excellent performance.[32–34] A previous study showed that NiCu electrocatalysts, by possessing a unique pine-needle-like dendrite nanotube morphology, can offer a relatively high electrochemical surface area (ECSA), which is essential for an active electrocatalyst;[35] nevertheless, the NiCu electrocatalyst displayed relatively high overpotentials to attain current densities of 10 (203 mV) and 100 mA cm^{-2} (310 mV) for HER.[36] Consequently, NiCu needs to improve its catalytic properties further. Various transition metal sulfide (TMS) electrocatalysts (e.g., MoS_2, Co_3S_4, and FeS_2) have been considerably investigated and their potential as OER, UOR, and HER catalysts has been demonstrated. In the past few years, some TMS have exhibited activities that are closer to those of platinum group electrocatalysts due to modifications, such as surface engineering, phase control, and composition regulation.[37] However, there are still many challenges for TMSs, including poor structural stability and poor electrical conductivity, especially in oxi-

dation reactions (i.e., under oxidation potentials).[38] To overcome the shortcomings mentioned above, the fabrication of bimetallic TMSs, such as NiCoS,[39] CoMoS,[40] $MnCo_2S_4$,[41] NiFeS,[42] and NiMnS,[43] have been proven to be a practical approach. Bimetallic TMSs have been found to exhibit enhanced catalytic activity compared to their monometallic counterparts, which can be attributed to their improved electrical conductivity, lower band-gap energy, high active sites, and more adjustable oxidation states.[38] Nevertheless, bimetallic TMSs still suffer from slow reaction kinetics.[44] Therefore, it is necessary to overcome the challenge by further improving the activity of these catalytic compounds. The use of heterostructures has many advantages for catalytic applications. Some of their numerous benefits are that they can optimize the electronic structure, consequently increasing the electrical conductivity and kinetic reactions by creating a synergistic effect between other existing structures, which is essential for an electrocatalyst.[45] Additionally, fabricating heterostructured electrocatalysts is an impressive method to increase the number of active sites. Most electrocatalysts with heterostructures have refined nanostructures with substantially exposed edges, which offer abundant adsorption sites for reaction intermediates.[45–47] Also, the manufacturing process of a high-efficiency catalyst is of great importance for the commercialization of a high-efficiency catalyst. This method should be fast, easy, and efficient. Methods based on electrochemical deposition procedures are of this category that can provide suitable morphologies with high electrochemical surface area in addition to suitable intrinsic catalytic properties.

In this work, a three-dimensional Ni–Mn–S/Ni–Cu heterostructure was grown on nickel foam (NF) using a two-step electrochemical deposition procedure. The optimized sample (Ni–Mn–S/Ni–Cu/10) exhibits HER activity, with a low overpotential of 64 mV at 10 mA cm^{-2} and a Tafel slope of 81 mV dec^{-1} in 1.0 M KOH solution. The Ni–Mn–S/Ni–Cu/10 catalyst has a very low potential of 1.247 V vs. RHE for 10 mA cm^{-2} toward UOR in an electrolyte containing 1.0 M KOH + 0.33 M urea. Furthermore, the sample demonstrated remarkable stability, with sustained potential at a current density of 100 mA cm^{-2} for both HER and UOR over 24 h. Ni–Mn–S/Ni–Cu/10 demonstrated unexpected overall urea–water electrolysis activity, requiring 1.302 V to drive 10 mA cm^{-2} with long-term performance (24 h at 100 mA cm^{-2}). Developing a Ni–Mn–S/Ni–Cu nanostructure as a bi-functional electrocatalyst for HER-UOR presents a promising opportunity to achieve an affordable and energy-efficient hydrogen production process in the future.

2. Experimental details

2.1. Fabrication of electrocatalysts

At first, in this study, Ni–Cu nano microdendrites were created on the nickel foam (NF) surface. The NF electrodes were first cut into the desired dimensions (1 × 1 cm^2). In the first step,

the NF samples were degreased with acetone in an ultrasonic bath for 15 minutes and then placed in 1.0 M HCl solution for 1 minute to remove the surface oxides and then washed with distilled water. For the process of electrochemical deposition at this stage, a two-electrode cell was used, and a graphite rod was used as the anode. The composition of the coating solution is given in Table S1.† The deposition current density was equal to 2 A cm^{-2}, and the deposition time was equal to 100 seconds. In the second step, Ni–Mn–S nanowires were created by the CV electrodeposition method in different numbers of cycles on the surface of Ni–Cu nano–micro dendrites. The composition of the solution for electrochemical deposition is given in Table S2.† A three-electrode cell was used for deposition in this step, in which the Ni–Cu electrode was used as the working electrode, Ag/AgCl electrode as a reference, and graphite rod as a counter electrode. The potential range was −0.2 to −1.3 V vs. Ag/AgCl, and the scan rate was 20 mV s^{-1}. The number of coating cycles was considered as variable and equal to 3, 5, 10, and 20 cycles. After coating, the samples were washed several times with distilled water and prepared for tests.

2.2. Characterization

From the morphological and chemical composition point of view of the samples, they were examined by a field emission-scanning electron microscope (FESEM, MIRA 3 TESCAN), which was equipped with an energy dispersive spectroscopy (EDS) analyzer. The surface chemistry of the samples was also analyzed by X-ray photoelectron spectroscopy (XPS) (Thermo-Scientific ESCALAB 250Xi). More detailed analyses regarding the structure and morphology were also done by transmission electron microscopy and high-resolution transmission electron microscopy (TEM and HRTEM, JEOL JEM-2100).

An electrochemical workstation ZIVE SP1 was used for all electrochemical tests. To check the electrochemical activity of all the samples for the HER process, the linear sweep voltammetry (LSV) test was used with a scan rate of 5 mV s^{-1} in a three-electrode cell in a 1.0 M KOH solution, in which the electrodes synthesized were used as the working electrode, Ag/AgCl electrode worked as the reference electrode and graphite rod as the counter electrode. Also, the solution used to investigate the electrochemical activity in the UOR process was 1.0 M KOH + 0.33 M urea. The electrochemical impedance spectroscopy (EIS) test was conducted in the frequency range from 100 kHz to 100 mHz at different potentials to investigate the mechanism and kinetics of electrochemical processes. The cyclic voltammetry (CV) test was used in the non-faradaic current range to obtain the C_{dl} value. Electrocatalytic stability was also assessed through the chronopotentiometry test.

3. Results and discussion

3.1. Characterization of electrocatalysts

The synthesis of three-dimensional Ni–Mn–S/Ni–Cu nanostructure electrocatalysts was achieved on the NF substrate using a two-step electrodeposition method. This method was used due to its simplicity, cost-effectiveness, and low synthesis time. Initially, an Ni–Cu substrate was produced using the galvanostatic method at a consistent current density of 2 A cm^{-2} for 100 s on the NF substrate (Ni–Cu/NF). Next, the Ni–Mn–S coating was deposited on the Ni–Cu/NF (Ni–Mn–S/Ni–Cu) using the CV technique, and the impact of varying the number of cycle parameters (3, 5, 10, and 20) on the catalyst morphology was investigated. The TEM image after the first step of the electrochemical deposition process (Ni–Cu/NF) is shown in Fig. 1a. Based on the TEM image, the dark region exhibits a micro–nano dendrite structure, which can be attributed to the single phase of Ni–Cu. Furthermore, the edge of the micro–nano dendrites appears rough. The three-dimensional micro–nano dendrite structure of the Ni–Cu/NF substrate was created using the dynamic hydrogen bubble template (DHBT) method, which is a cost-effective, efficient, and easily controllable technique, also forming porous films with high surface areas.[48–51] In the DHBT, two processes take place on the cathode surface. These processes include the deposition of nickel and copper as well as the hydrogen evolution reaction. In the process of DHBT, the generation of hydrogen bubbles plays a crucial role in the development of the Ni–Cu layer. When electrodeposition occurs at a high overpotential, an oversaturation of hydrogen near the NF electrode causes the formation of small and irregular bubbles on the electrode surface. These bubbles block the active sites of the NF surface, driving metallic ions to find alternative deposition sites around them and forming a porous structure. As these small bubbles combine and grow, they form larger bubbles in the layers of the Ni–Cu coating. When these larger bubbles reach a critical size, they detach from the electrode surface, making holes in the deposited layer. Then, the Ni–Cu layer deposition occurs around these bubbles, which effectively acts as a dynamic template. It must be noted that the kinetics of the hydrogen evolution reaction on the substrate have a direct impact on the rate of bubble formation and detachment. Consequently, this interaction significantly affects the size, morphology, and porosity of the deposited layer.[48–51] The micro–nano dendrite structure is formed when the electrochemical deposition process is under diffusion control and high current density is applied.

At first, multiple nuclei form on the NF surface. The process then advances as new nickel and copper atoms are adsorbed onto the surface of the initial nuclei (the primary clusters). As time progresses, the newly deposited particles are more likely to adhere to the tip of the clusters and other parts of the clusters, leading to external growth and the formation of secondary clusters. Furthermore, as the deposition continues, tertiary clusters grow on the surface of the secondary clusters, eventually resulting in the formation of the final dendritic structure.[52] Fig. S1† and Fig. 1(b and c) display the FESEM images of Ni–Mn–S/Ni–Cu electrocatalysts with different cycles, including 3, 5, 20, and 10 cycles (optimized sample). The FESEM images confirm that the morphology of Ni–Mn–S nanowires changes significantly with the deposition cycles. Based on the images presented in Fig. S1a and b,† the mor-
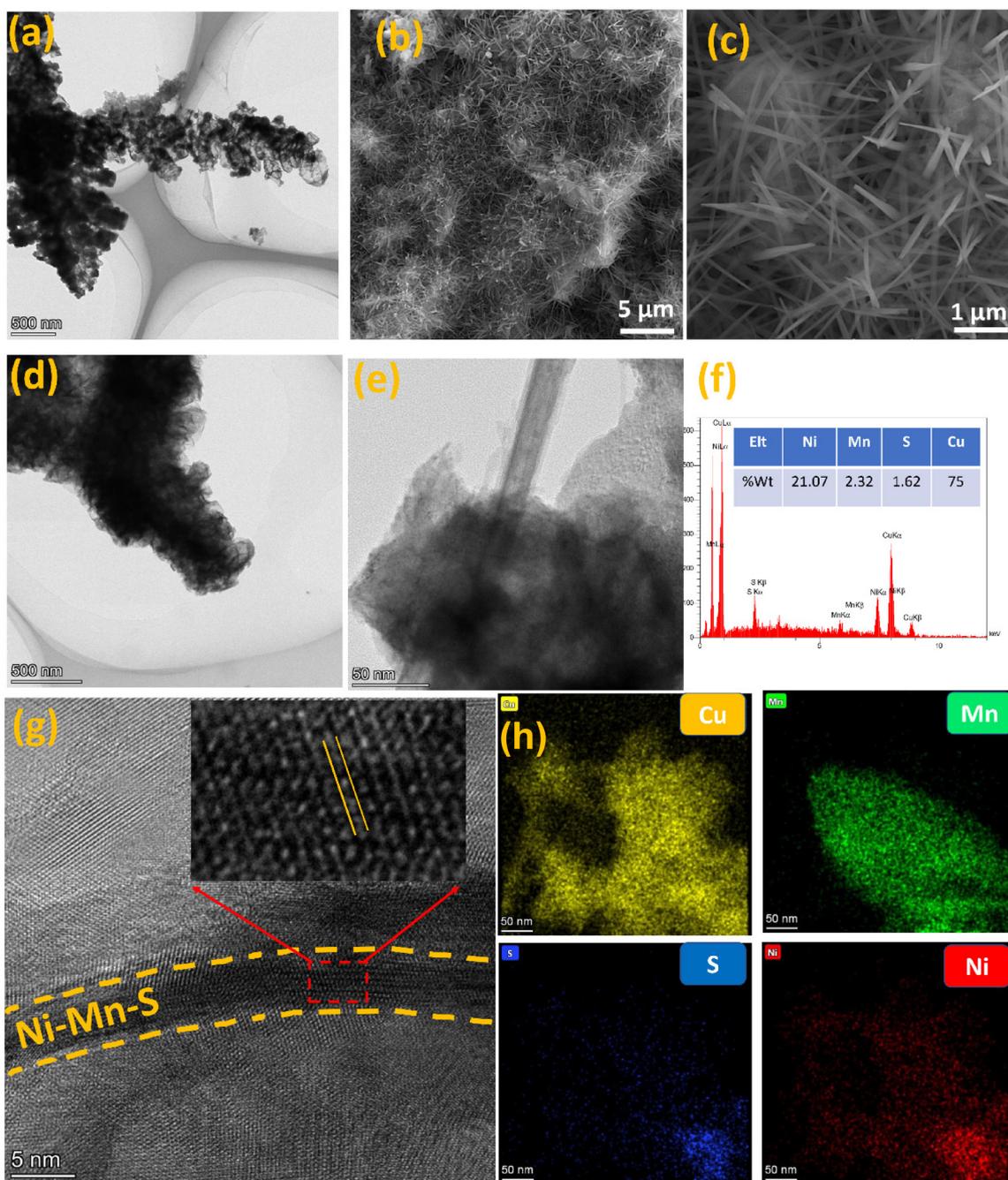
Fig. 1 (a) TEM image of Ni–Cu micro–nano dendrite, (b) and (c) low and high magnification FESEM images of Ni–Mn–S/Ni–Cu/10 nanowire, (d) and (e) TEM images of Ni–Mn–S/Ni–Cu/10 nanowire, (f) EDX analysis, (g) HRTEM image, and (h) TEM-elemental mapping of Ni–Mn–S/Ni–Cu/10 nanowire.

pholcogy of the samples obtained during cycles 3 and 5 remains fairly consistent and dendritic. The observed phenomenon can be attributed to the presence of an Ni–Cu layer on the NF substrate and the low concentration of Ni–Mn–S nanowires. Additionally, the limited number of nanowires can be attributed to fewer cycles, resulting in low opportunities for their formation. In the optimized sample, as shown in Fig. 1b and c, the electrode is presented through low and high-magni-

fication FESEM images. These images illustrate the uniform growth of the three-dimensional morphology of Ni–Mn–S nanowires, with an average size of approximately 1 μm, covering the Ni–Cu micro–nano dendrite uniformly. With an increase in the number of cycles, the loading of Ni–Mn–S increased, which adversely affected the catalyst's morphology. Specifically, in the sample created with 20 cycles (as depicted in Fig. S1c†), the nanowire density is higher, resulting in a

thicker and more uniform outer layer. However, this denser morphology also decreases the porous nature of the material, leading to a lower active surface area and decrease in the electrocatalytic performance. It must be mentioned that the TEM images of the Ni–Mn–S/Ni–Cu/10 sample (Fig. 1d and e) are composed of Ni–Mn–S nanowires on the Ni–Cu micro–nano dendrites; this structure increases the surface area and provides more active sites, which is compatible with the findings from the FESEM images. Based on the results of the energy-dispersive X-ray spectroscopy (EDX) analysis, the Ni–Mn–S/Ni–Cu electrocatalysts exhibit a uniform composition of nickel, manganese, sulfur, and copper, as evidenced by the images depicted in Fig. S1† and Fig. 1f. Specifically, the optimized sample contains 21.07% nickel, 2.32% manganese, 1.62% sulfur, and 75% copper. Fig. 1g displays an HRTEM image in which a yellow dashed line marks the Ni–Mn–S phase. Through the HRTEM image, it can be confirmed that the Ni–Mn–S nanowires have a crystalline nature and uniform distribution. The lattice fringe spacing of 0.341 nm was measured for the Ni–Mn–S phase, which corresponds to the mixture of sulfides, including the (200) planes of α-MnS and the (220) planes of Ni_3S_4.[53,54] TEM elemental mapping of the Ni–Mn–S/Ni–Cu/10 sample displays the distribution of Cu, Mn, S, and Ni elements (Fig. 1h). The results indicate that these elements are homogeneously distributed throughout the sample, and the EDX analysis supports this.

X-ray photoelectron spectroscopy (XPS) analysis was conducted to evaluate the surface chemical compositions and elemental valence states of the optimized sample. The obtained spectrum confirms the presence of nickel, copper, manganese, and sulfur elements in the Ni–Mn–S/Ni–Cu/10 sample, which is consistent with the EDX and TEM-elemental mapping results. In Fig. 2a, a detailed Ni 2p spectrum with four distinct peaks is visible. Specifically, these peaks represent Ni $2p_{3/2}$ with a binding energy of 855 eV, Ni $2p_{1/2}$ with a binding energy of 873 eV, and satellite peaks at 862 and 879 eV (identified as "sat"). Notably, the peaks located at 855 and 873 eV suggest the presence of Ni^{2+} species on the substrate's surface.[55–59] As depicted in Fig. 2b, the XPS spectrum of Cu 2p clearly shows two main peaks, namely, Cu $2p_{3/2}$ and Cu $2p_{1/2}$. The peaks observed at 932 and 952 eV are linked to Cu $2p_{3/2}$ and Cu $2p_{1/2}$ of CuO, while the peaks at 934 and 955 eV suggest the presence of Cu $2p_{3/2}$ and Cu $2p_{1/2}$ for Cu^{2+}. A weak satellite peak was also detected at a binding energy of 942 eV. The intensity of Cu^{2+} peaks is noticeably lower than that of CuO, indicating the slight oxidation of copper in the Ni–Cu layer.[60,61] The Mn 2p spectrum displays just one peak, which can be attributed to the Mn $2p_{3/2}$ state (as depicted in Fig. 2c). Based on peak deconvolution analysis, the peaks positioned at 640 and 650 eV are related to Mn^{2+} and the one at 643 eV is assigned to Mn^{3+}.[62–66] As revealed in Fig. 2d, the S 2p spectrum exhibited two peaks, one at a lower binding energy and
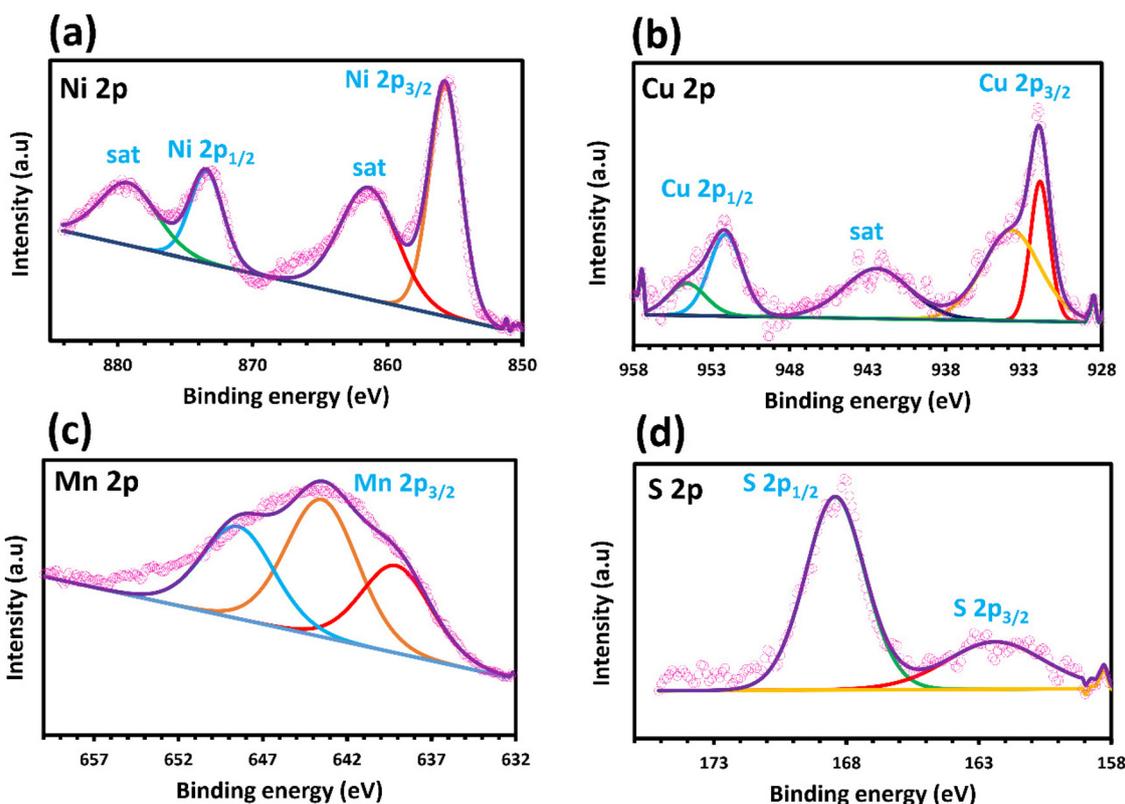

Fig. 2 High-resolution XPS spectra of Ni–Mn–S/Ni–Cu/10 nanowire: (a) Ni 2p, (b) Cu 2p, (c) Mn 2p, and (d) S 2p.

another at a higher binding energy. The sample contains metal–sulfur bonding with a peak at 162 eV ascribed to the S $2p_{3/2}$ of S^{2-} and the peak at 168 eV ascribed to the oxidized sulfur.[66–70]

3.2. Electrocatalytic performance

3.2.1 HER performance. To investigate the effect of different cycles of electrodeposition on the catalytic activity of Ni–Mn–S/Ni–Cu and compared with the Ni–Cu substrate and Pt (the fabrication method is based on our previous study[71]), the electrocatalytic performance of the as-prepared samples was evaluated toward HER using a typical three-electrode system in 1.0 M KOH (Fig. 3). The obtained raw results were iR corrected to reflect the intrinsic activities of all the samples. Fig. 3a illustrates the linear sweep voltammetry (LSV) curves of Ni–Mn–S/Ni–Cu for 3, 5, 10, and 20 cycles along with Ni–Cu and Pt electrocatalyst in 1.0 M KOH with a scan rate of 5.0 mV s^{-1} for HER. As can be seen, the Ni–Mn–S/Ni–Cu electrode pre-

pared in 10 cycles (Ni–Mn–S/Ni–Cu/10) with overpotentials of 64 mV and 160 mV to reach current densities of 10 and 100 mA cm^{-2}, respectively, has the best performance among the samples synthesized in 3 cycles (107 and 250 mV at 10 and 100 mA cm^{-2}, respectively), 5 (104 and 228 mV at 10 and 100 mA cm^{-2}, respectively), and 20 (71 and 190 mV at 10 and 100 mA cm^{-2}, respectively). Ni–Mn–S/Ni–Cu/10 had a similar catalytic performance to the Pt electrode and a much better catalytic activity than its Ni–Cu substrate, which needs much higher overpotentials of 186 and 345 mV to reach 10 and 100 mA cm^{-2}, respectively.

Evidently, the number of electrodeposition cycles significantly influenced the electrode's microstructure and morphology. Consequently, by changing the number of electrodeposition cycles, the electrocatalytic activity and HER performance will be altered. LSV curves demonstrate that changing the cycles of electrodeposition from 3 cycles to 10 cycles causes a drop in η_{10} from 107 mV to 64 mV, implying an enhancement in the HER activity. In addition, increasing the electrodeposition cycles from 10 to 20 cycles results in an increase in the η_{10} to 71 mV, demonstrating an undesirable effect on the catalytic activity. As a result, it can be concluded that the Ni–Mn–S/Ni–Cu/10 electrode has the highest electrocatalytic performance among other as-prepared electrodes. An efficient electrocatalyst should possess a high activity in both high and low current densities. The LSV results for Ni–Mn–S/Ni–Cu/10 indicate that this electrode needs only a low potential of 160 mV to reach a high current density of 100 mA cm^{-2}, which is much better than that of the other as-prepared electrodes reported in Table S3.† In addition, the catalytic activity of Ni–S and Mn–S along with Ni–Mn–S under the optimized conditions is illustrated in Fig. S2.† As can be seen, the catalytic activity of Ni–Mn–S is better than that of Ni–S (η_{10} = 127) and Mn–S (η_{10} = 149). Thus, the synergetic effect of different sulfide-based phases contributes to the improvement of the catalytic activity. Thus, the introduction of Mn can regulate the electronic structure and change the electrochemical properties of the fabricated catalyst by adjusting the adsorption free energy of the intermediates of the reactions. Moreover, it is reported that Mn doping can accelerate the electron transfer.[72] Moreover, to evaluate the HER mechanism and kinetics, the Tafel slope curves obtained from their LSV plots (Fig. 3a) are illustrated in Fig. 3b. The Tafel slopes were analyzed to clarify how hydrogen is produced by the electrodes and examine the kinetics involved. The Tafel analysis indicates that three distinct stages can occur for the hydrogen evolution reaction in an alkaline environment: Volmer (the electrochemical adsorption of hydrogen atoms), Heyrovsky (the electrochemical desorption of hydrogen molecules), and Tafel (the chemical desorption of hydrogen molecules). When the Tafel slope measures approximately 120, 40, and 30 mV dec^{-1}, the Volmer, Heyrovsky, and Tafel reactions serve as the rate-determining steps (RDS) of the HER, respectively. A reduced Tafel slope indicates that a smaller overpotential is required to raise the current density.[74,75] In Fig. 3b, the Tafel slopes for the synthesized electrodes are as follows: Ni–Mn–S/Ni–Cu/3 shows a slope of
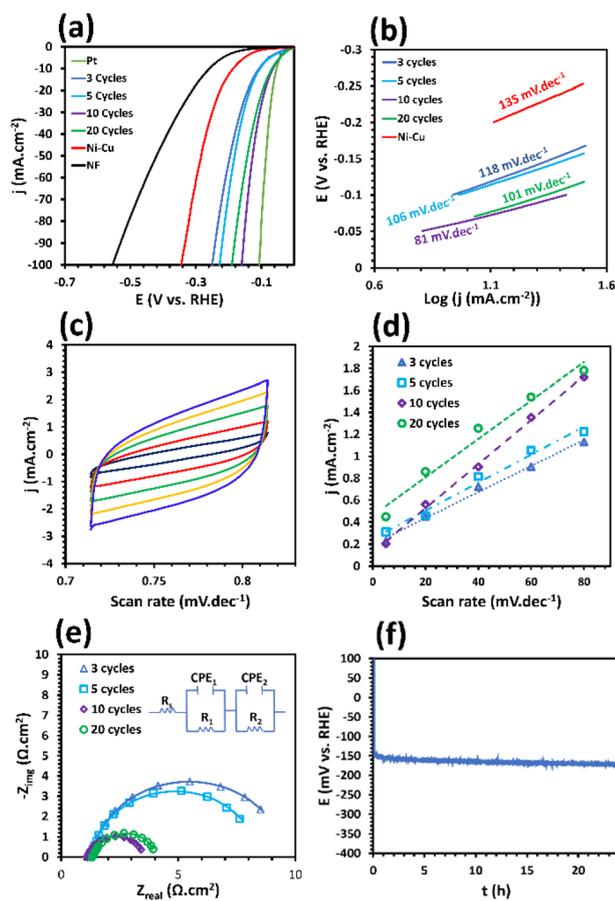

Fig. 3 (a) and (b) LSV and corresponding Tafel curves of Ni–Mn–S/Ni–Cu nanowires fabricated at different cycles for HER in 1.0 M KOH solution, (c) CV curves at different scan rates in the non-faradaic current region of the Ni–Mn–S/Ni–Cu/10 sample, (d) current density as a function of scan rate, and (e) Nyquist plots of different samples (inset: the electrical equivalent circuit utilized for fitting the EIS data). (f) CP curve for the evaluation of the electrocatalytic stability at an applied current density of 100 mA cm^{-2} for Ni–Mn–S/Ni–Cu/10.

118 mV dec^{-1}, Ni–Mn–S/Ni–Cu/5 exhibits a slope of 106 mV dec^{-1}, Ni–Mn–S/Ni–Cu/10 presents a slope of 81 mV dec^{-1}, and Ni–Mn–S/Ni–Cu/20 has a slope of 101 mV dec^{-1}. These values suggest that all electrodes follow the Volmer–Heyrovsky mechanism. Furthermore, the Tafel slope value for Ni–Mn–S/Ni–Cu/10 is significantly lower than that of its Ni–Cu substrate, which is 135 mV dec^{-1}. This reduced Tafel slope for Ni–Mn–S/Ni–Cu/10 signifies enhanced kinetic performance compared to the other electrocatalysts produced, which likely results from a synergistic interaction between the Ni–Mn–S and Ni–Cu layers. This synergistic effect can improve and optimize the electronic structure within the electrode and increase the electrical conductivity. Another noticeable factor that could play a key role in enhancing the reaction kinetics is the nanoneedle-like morphology of the Ni–Mn–S/Ni–Cu/10 electrode.

These nanoneedles of Ni–Mn–S/Ni–Cu/10, by creating superaerophobic properties, can easily adsorb active species within the electrolyte due to the immediate detachment of gas bubbles. Markedly, the figures of the Tafel slope for Ni–Mn–S/Ni–Cu/10 reveal the fact that the HER rate-determining stage on Ni–Mn–S/Ni–Cu/10 is the desorption of atomic hydrogen from the surface (Volmer–Heyrovsky mechanism).[1] The double-layer capacitance (C_{dl}) is another important factor that can reflect the intrinsic properties of an electrocatalyst by representing its electrochemical surface area. Fig. 3d demonstrates the C_{dl} values of the Ni–Mn–S/Ni–Cu samples prepared in different cycles. The C_{dl} value of Ni–Mn–S/Ni–Cu/10 (20.1 mF cm^{-2}), which is obtained from its CV curves in Fig. 3c, is higher than that of the samples prepared in 3 (11.9 mF cm^{-2}), 5 (12.8 mF cm^{-2}), and 20 (17.5 mF cm^{-2}) cycles. According to the C_{dl} value for Ni–Mn–S/Ni–Cu/10, a larger electrochemical surface area and consequently higher catalytic active sites can be expected. The higher double-layer capacitance value for the Ni–Mn–S/Ni–Cu/10 electrocatalyst could be related to the high nanoneedle density in its morphology.

For the more insightful analysis of the HER kinetics, electrochemical impedance spectroscopy (EIS) was utilized at 200 mV overpotential *vs.* RHE for the as-mentioned catalysts in 1.0 M KOH (Fig. 3e). The Nyquist curve plot presents a unique depressed semicircle shape in all the samples, which clearly reveals that hydrogen production is controlled by charge transfer. For fitting the data, an electrical equivalent circuit (EC) with a two-time constant was utilized (Fig. 3e). In this circuit, R_s defines the solution resistance; the first (CPE_1 and R_1) and second time constant (CPE_2 and R_2) at high and low frequencies, respectively, are attributed to the porosity and charge transfer process of the electrode. The data depicted in Fig. 3e confirm that the semicircles exhibit no noticeable variation at high frequencies; therefore, the samples share the same surface porosity. The charge transfer resistance (R_2) can be accurately determined by measuring the diameter of the semicircles present in the Nyquist plot for the Ni–Mn–S/Ni–Cu electrodes at low frequencies. The R_2 value for Ni–Mn–S/Ni–Cu/10 is 1.9 Ω cm^2, which is lower than that of other samples and in agreement with the obtained results from the Tafel slope

results. The EIS results prove that the Ni–Mn–S/Ni–Cu/10 sample has better catalytic activity and electrical conductivity than the other samples. In addition, the Nyquist plots at different overpotentials (100, 200 and 300 mV) are represented in Fig. S3.† It can be seen that by increasing the overpotentials, the charge transfer resistance decreases, which means better HER kinetics at higher overpotentials. The electrocatalytic stability of the Ni–Mn–S/Ni–Cu/10 electrode for the hydrogen evolution reaction was assessed using chronopotentiometry (CP) with a current density of −100 mA cm^{-2}, and the result is depicted in Fig. 3f. Following 24 h of electrolysis, the overpotential displays minimal changes, with the potential level remaining almost consistent, which suggests that the optimized sample boasts exceptional electrocatalytic stability.

In addition, the catalytic activity is severely affected by the behaviour of bubble detachment during electrochemical gas-evolving reactions.[73] Here, the EIS data at fixed frequency (dynamic specific resistance test) were obtained for understanding the changes in the IZI resulting from the behaviour of bubble detachment. The test was done in −50 mA cm^{-2} and 1 Hz frequency for 600 seconds. As can be seen in Fig. S4,† the fluctuation in IZI is not high, which means the rapid detachment of the formed bubble during electrochemical hydrogen production and consequently indicates the low bubble resistance.

3.2.2. UOR performance. The high overpotential required for the overall water splitting (OWS) process can be attributed to the sluggish kinetics associated with the four-stage charge transfer process in OER. In light of this, it is essential to explore alternative oxidation reactions with lower thermodynamic potentials. One such alternative is the UOR, which can substitute the OER process and reduce the cell voltage to lower values. For evaluating the electrocatalytic behavior of Ni–Mn–S/Ni–Cu samples for the UOR process, LSV curves were also assessed in 1.0 M KOH + 0.33 M urea solution with a scan rate of 5 mV s^{-1}. As shown in Fig. 4a, it is evident that the Ni–Mn–S/Ni–Cu/10 catalyst displays an optimal UOR catalytic activity, where only 1.238 and 1.372 V *vs.* RHE are needed to drive the current density of 10 and 100 mA cm^{-2}, respectively, lower than that of other electrodes. Moreover, deriving Tafel slopes through the fitting of LSV plots facilitated the evaluation of the reaction kinetics of the electrocatalysts. As shown in Fig. 4b, the Tafel slopes recorded for the samples prepared in 3, 5, 10, and 20 cycles were 82, 70, 87, and 162 mV dec^{-1}, respectively. These results highlight the rapid and highly favorable kinetics of the urea oxidation reaction (UOR) for the Ni–Mn–S/Ni–Cu electrodes. Importantly, these Tafel slopes are considerably lower than those reported for other electrodes utilized in UOR, as detailed in Table S4,† further supporting the excellent performance of the Ni–Mn–S/Ni–Cu configuration.

The outstanding performance of Ni–Mn–S/Ni–Cu/10 for the UOR process can be attributed to the synergistic interaction between elements, high electrical conductivity, high active surface area, and binder-free electrode formation, which results in low potential and good kinetics. In order to examine the efficacy of UOR as a promising alternative to OER, a com-
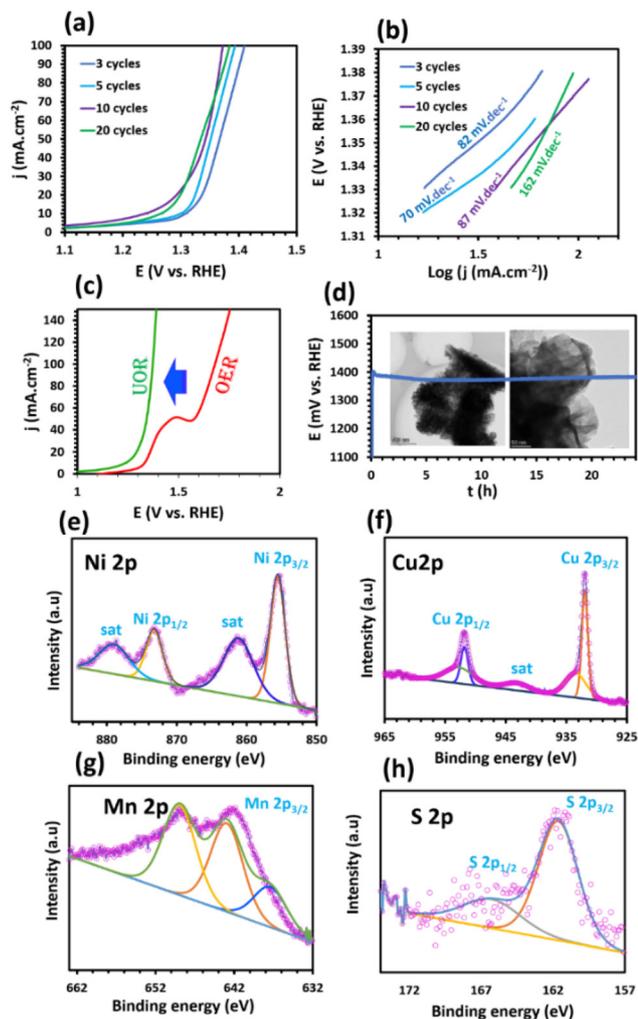
Fig. 4 (a) and (b) LSV and corresponding Tafel curves of the electrodes fabricated at different cycles for UOR in 1.0 M KOH + 0.33 M urea solution, (c) comparison of OER and UOR of the Ni–Mn–S/Ni–Cu/10 sample, (d) CP curve for the evaluation of the electrocatalytic stability of the optimized sample at 100 mA cm^{-2} (TEM images after the stability test). High-resolution XPS spectra of the Ni–Mn–S/Ni–Cu/10 sample after the UOR stability test: (e) Ni 2p, (f) Cu 2p, (g) Mn 2p, and (h) S 2p.

parison between the two was conducted for the optimized electrode. The results of this comparison can be observed in Fig. 4c, which clearly illustrates the differences in the efficiency and performance of both processes. The UOR process requires an onset potential significantly lower than that of the OER process. The voltage essential to achieve a current density of 100 mA cm^{-2} for the Ni–Mn–S/Ni–Cu/10 sample in the OER process is 1.680 V *vs.* RHE, which is notably 308 mV higher than the voltage requirements for the UOR process. Moreover, the comparison of Ni–Mn–S/Ni–Cu/10 over some reported electrocatalysts also displays superior electrocatalytic performance for UOR (Table S4†).

For energy-conversion systems, the long-term stability of catalysts is a critical factor. Long-term chronopotentiometry technique was performed at a consistent current density of

100 mA cm^{-2} for over 24 h in 1.0 M KOH + 0.33 M urea solution. Fig. 4d shows that Ni–Mn–S/Ni–Cu/10 potential change is negligible during the operation, exhibiting remarkable electrocatalytic stability during the UOR process. In addition, the remarkable stability demonstrated by the electrodeposited layer can be attributed to its inherent morphological and chemical properties. To evaluate the morphological stability, the surface of the Ni–Mn–S/Ni–Cu/10 electrode was studied after the UOR electrocatalytic stability test using the TEM technique. By comparing the TEM images before (Fig. 1d and e) and after the stability test (Fig. 4d), after the 24 h stability test, the morphological structure of Ni–Mn–S/Ni–Cu/10 is excellently maintained. After the stability test, XPS spectra were used to investigate changes in the chemical composition and valence of different elements (Fig. 4e–h); the results indicate that no changes in the chemical composition were observed after the stability test, confirming its chemical stability and corrosion resistance in an alkaline environment. Throughout the stability test, exposure to harsh alkaline conditions and the detachment of gas bubbles can potentially lead to surface damage, ultimately weakening the electrocatalytic stability. Nonetheless, the nanostructure of the Ni–Mn–S/Ni–Cu/10 sample facilitates the swift detachment of gas bubbles from the surface, which in turn enhances the catalytic stability.

3.2.3. Overall urea–water electrolysis performance. Due to the superior performance of Ni–Mn–S/Ni–Cu/10 toward HER and UOR in the alkaline media without and with urea, respectively, a two-electrode electrolyzer constituting two Ni–Mn–S/Ni–Cu/10 electrodes as both anode and cathode (Ni–Mn–S/Ni–Cu/10||Ni–Mn–S/Ni–Cu/10) was constructed to further evaluate the overall urea–water electrolysis performance (HER-UOR). A schematic of the HER-UOR process is depicted in Fig. 5a. Moreover, the two-electrode system for OWS in 1.0 M KOH was also tested for comparison (HER-OER). Fig. 5b demonstrates the LSV curves of the Ni–Mn–S/Ni–Cu/10||Ni–Mn–S/Ni–Cu/10 in alkaline water solutions without and with 0.33 M urea. As observed in Fig. 5b, the bi-functional Ni–Mn–S/Ni–Cu/10 electrocatalyst displayed outstanding electrochemical performance with a low cell voltage of 1.302 V, which is required to yield 10 mA cm^{-2} in the presence of urea.

As expected, the OWS for the system requires a voltage of 1.443 V to attain 10 mA cm^{-2}, which is 141 mV higher than that of the overall urea–water splitting. This reveals that the Ni–Mn–S/Ni–Cu/10||Ni–Mn–S/Ni–Cu/10 configuration demonstrated high electrochemical performance for urea–water electrolysis and confirms replacing the sluggish OER with the thermodynamically favorable UOR to enhance the H$_2$ production yield. The cell performance of Ni–Mn–S/Ni–Cu/10 is comparable with that of previously studied electrocatalysts for overall urea electrolysis (Table S5†).

Moreover, the durability of the Ni–Mn–S/Ni–Cu/10||Ni–Mn–S/Ni–Cu/10 system in 1.0 M KOH + 0.33 M urea was studied by measuring the cell voltage at 50 mA cm^{-2} for 24 h (Fig. 5c). Throughout continuous running for 24 h, Ni–Mn–S/Ni–Cu/10 showed a slight change in the cell voltage and highly stable performance, which confirms the superior electrocatalytic
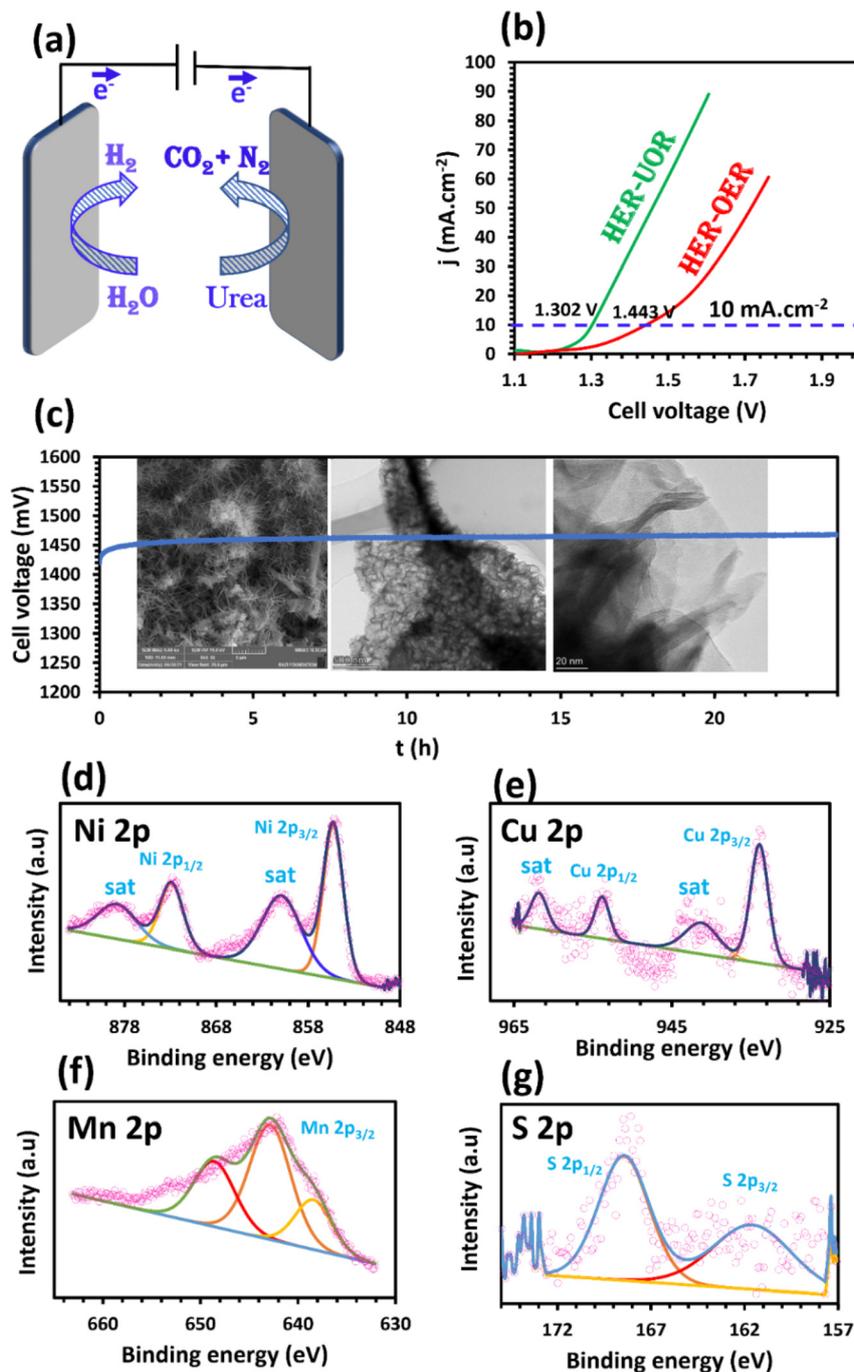
Fig. 5 (a) Schematic of overall urea–water splitting, (b) LSV curves of Ni–Mn–S/Ni–Cu/10||Ni–Mn–S/Ni–Cu/10 in 1.0 M KOH + 0.33 M urea and 1.0 M KOH solution for comparison, (c) evaluation of the electrocatalytic stability by CP at 100 mA cm^{-2} (FESEM and TEM images of Ni–Mn–S/Ni–Cu/10 after the stability test). High-resolution XPS spectra of the optimized sample after the stability test: (d) Ni 2p, (e) Cu 2p, (f) Mn 2p, and (g) S 2p.

stability of the optimized sample as a bi-functional electrode. Furthermore, FESEM, TEM, and XPS were also performed to understand the structural evolution of the electrode surface after the chronopotentiometry test. The FESEM and TEM images, after the stability test presented in Fig. 5c, show that the morphological structure of Ni–Mn–S/Ni–Cu/10 is excellently maintained, indicating its good structural stability towards urea–water electrolysis. Also, the XPS spectra of Ni 2p

(Fig. 5d), Cu 2p (Fig. 5e), Mn 2p (Fig. 5f), and S 2p (Fig. 5g) for Ni–Mn–S/Ni–Cu/10||Ni–Mn–S/Ni–Cu/10 cell after sustained operation at the current density of 100 mA cm^{-2} for 24 h demonstrate that there were no modifications to the composition of the electrode, confirming the chemical stability of the sample for the HER-UOR process. The exceptional stability and remarkable efficiency of the Ni–Mn–S/Ni–Cu/10 catalyst in urea–water electrolysis can be influenced by various factors.

Firstly, the cooperative effect of the Ni, Mn, S, and Cu elements in the electrode enhances the adsorption and desorption pathway of the electroactive species. Secondly, the synergistic effect between the two nanosheets of Ni–Mn–S/Ni–Cu provides direct and efficient electron pathways and minimizes the interfacial resistance. Thirdly, the three-dimensional morphology of the nanostructured sample presents numerous active sites, promoting the transfer of both mass and charge as well as the diffusion of the generated gases. Finally, the electrode design, produced without a binder through electrodeposition synthesis, provides superior adhesion capabilities and maintains the electroconductivity.

4. Conclusion

In conclusion, a micro–nanostructured Ni–Mn–S/Ni–Cu electrocatalyst was effectively synthesized on an NF substrate using a two-step electrodeposition process comprising galvanostatic electrodeposition and cyclic voltammetry. The surface investigation results have confirmed the successful production of the Ni–Mn–S/Ni–Cu samples, which exhibit coatings containing varying percentages of different elements. The electrochemical studies have confirmed that the synthesized electrodes are exceptional in their electrocatalytic activity for both HER and UOR processes. The optimized sample was created using 10 cycles in the CV test (Ni–Mn–S/Ni–Cu/10), which resulted in overpotentials of 64 mV at current densities of 10 mA cm^{-2} and a Tafel slope of 81 mV dec^{-1} for the HER process. Also, a potential of 1.238 V $vs.$ RHE was needed to generate a current density of 10 mA cm^{-2} during the UOR process. When Ni–Mn–S/Ni–Cu/10 was utilized as both the cathode and anode in the overall urea–water electrolysis system (Ni–Mn–S/Ni–Cu/10||Ni–Mn–S/Ni–Cu/10), the material displayed a low cell voltage of 1.302 V to achieve 10 mA cm^{-2} with remarkable stability (24 h at 100 mA cm^{-2}). It must be mentioned that the potential required was about 141 mV lower than that of OWS. The electrodes' impressive performance can be attributed to several factors, including low charge transfer resistance, high number of active sites, and a superaerophobic nature. This study highlights the impressive performance of the Ni–Mn–S/Ni–Cu nanostructure electrocatalyst, which was created through a straightforward, cost-effective, and binder-free method. This electrocatalyst exhibits tremendous potential as a substitute for noble metal catalysts, delivering efficient catalytic performance for both HER and UOR reactions.

Data availability

The data supporting this article have been included as part of the ESI.†

Conflicts of interest

There are no conflicts to declare.

References

1 J. O. Abe, A. Popoola, E. Ajenifuja and O. M. Popoola, *Int. J. Hydrogen Energy*, 2019, **44**, 15072–15086.

2 M. Momirlan and T. Veziroglu, *Renewable Sustainable Energy Rev.*, 2002, **6**, 141–179.

3 Y. Xu and B. Zhang, *ChemElectroChem*, 2019, **6**, 3214–3226.

4 S. Paygozar, A. Sabour Rouhaghdam, A. Seif and G. Barati Darband, *J. Mater. Chem. A*, 2024, **12**, 27558–27569.

5 M. Nazemi, G. B. Darband and A. Davoodi, *Nanoscale*, 2024, **16**, 10853–10863.

6 A. Buttler and H. Spliethoff, *Renewable Sustainable Energy Rev.*, 2018, **82**, 2440–2454.

7 B. K. Boggs, R. L. King and G. G. Botte, *Chem. Commun.*, 2009, 4859–4861.

8 C. Tang, R. Zhang, W. Lu, Z. Wang, D. Liu, S. Hao, G. Du, A. M. Asiri and X. Sun, *Angew. Chem., Int. Ed.*, 2017, **56**, 842–846.

9 X. Ma, J. Wang, D. Liu, R. Kong, S. Hao, G. Du, A. M. Asiri and X. Sun, *New J. Chem.*, 2017, **41**, 4754–4757.

10 Z. Hu, M. Wu, Z. Wei, S. Song and P. K. Shen, *J. Power Sources*, 2007, **166**, 458–461.

11 X. Hu, J. Zhu, J. Li and Q. Wu, *ChemElectroChem*, 2020, **7**, 3211–3228.

12 R. Andaveh, A. Sabour Rouhaghdam, A. Seif, K. Wang, M. Maleki, J. Ai, G. Barati Darband and J. Li, *ACS Appl. Mater. Interfaces*, 2024, **16**, 8717–8732.

13 A. Sanz-Cobena, T. H. Misselbrook, A. Arce, J. I. Mingot, J. A. Diez and A. Vallejo, *Agric., Ecosyst. Environ.*, 2008, **126**, 243–249.

14 E. Urbańczyk, M. Sowa and W. Simka, *J. Appl. Electrochem.*, 2016, **46**, 1011–1029.

15 M. Rahimpour, H. Mottaghi and M. Barmaki, *Fuel Process. Technol.*, 2010, **91**, 600–612.

16 M. Liu, Y. Jiao, S. Zhan and H. Wang, *Catal. Today*, 2020, **355**, 596–601.

17 C. Wang, Y. Sun, E. Tian, D. Fu, M. Zhang, X. Zhao and W. Ye, *Electrochim. Acta*, 2019, **320**, 134597.

18 P. Wang, X. Zhang, J. Zhang, S. Wan, S. Guo, G. Lu, J. Yao and X. Huang, *Nat. Commun.*, 2017, **8**, 14580.

19 W.-J. Jiang, T. Tang, Y. Zhang and J.-S. Hu, *Acc. Chem. Res.*, 2020, **53**, 1111–1123.

20 S. Ye, F. Luo, Q. Zhang, P. Zhang, T. Xu, Q. Wang, D. He, L. Guo, Y. Zhang and C. He, *Energy Environ. Sci.*, 2019, **12**, 1000–1007.

21 Y.-R. Liu, X. Shang, W.-K. Gao, B. Dong, X. Li, X.-H. Li, J.-C. Zhao, Y.-M. Chai, Y.-Q. Liu and C.-G. Liu, *J. Mater. Chem. A*, 2017, **5**, 2885–2896.

22 H. Wang, H. Zou, Y. Liu, Z. Liu, W. Sun, K. A. Lin, T. Li and S. Luo, *Sci. Rep.*, 2021, **11**, 21414.

23 H. Xu, K. Ye, K. Zhu, Y. Gao, J. Yin, J. Yan, G. Wang and D. Cao, *ACS Sustainable Chem. Eng.*, 2020, **8**, 16037–16045.

24 J. Xie, W. Liu, F. Lei, X. Zhang, H. Qu, L. Gao, P. Hao, B. Tang and Y. Xie, *Chem. – Eur. J.*, 2018, **24**, 18408–18412.

25 C. Tang, N. Cheng, Z. Pu, W. Xing and X. Sun, *Angew. Chem.*, 2015, **127**, 9483–9487.

26 H. Kato, K. Asakura and A. Kudo, *J. Am. Chem. Soc.*, 2003, **125**, 3082–3089.

27 J. Niu, Y. Yue, C. Yang, Y. Wang, J. Qin, X. Zhang and Z.-S. Wu, *Appl. Surf. Sci.*, 2021, **561**, 150030.

28 W. Zhang, D. Li, L. Zhang, X. She and D. Yang, *J. Energy Chem.*, 2019, **39**, 39–53.

29 L.-A. Stern, L. Feng, F. Song and X. Hu, *Energy Environ. Sci.*, 2015, **8**, 2347–2351.

30 H. Yan, S. Yao, T. Zhang, D. Li, X. Tang, M. Chen, Y. Zhou, M. Zhang, Y. Liu and X. Zhou, *Appl. Catal., B*, 2022, **306**, 121138.

31 D. Khalafallah, M. Zhi and Z. Hong, *ChemCatChem*, 2021, **13**, 81–110.

32 Q. Hu, J. Huang, G. Li, J. Chen, Z. Zhang, Z. Deng, Y. Jiang, W. Guo and Y. Cao, *Appl. Surf. Sci.*, 2016, **369**, 201–206.

33 X. Yu, X. Zhang, S. Wang and G. Feng, *Appl. Surf. Sci.*, 2015, **343**, 33–40.

34 C. Wang, Q. Hu, J. Huang, C. Zhu, Z. Deng, H. Shi, L. Wu, Z. Liu and Y. Cao, *Appl. Surf. Sci.*, 2014, **292**, 161–164.

35 S. Sun, H. Li and Z. J. Xu, *Joule*, 2018, **2**, 1024–1027.

36 N. Lotfi, T. S. Farahani, Y. Yaghoubinezhad and G. B. Darband, *Int. J. Hydrogen Energy*, 2019, **44**, 13296–13309.

37 Y. Zheng, Y. Jiao, M. Jaroniec and S. Z. Qiao, *Angew. Chem., Int. Ed.*, 2015, **54**, 52–65.

38 Y. Guo, T. Park, J. W. Yi, J. Henzie, J. Kim, Z. Wang, B. Jiang, Y. Bando, Y. Sugahara and J. Tang, *Adv. Mater.*, 2019, **31**, 1807134.

39 W. Liu, L. Dai, Y. Hu, K. Jiang, Q. Li, Y. Deng, J. Yuan, J. Bao and Y. Lei, *Inorg. Chem. Front.*, 2021, **8**, 4528–4535.

40 S. Shit, W. Jang, S. Bolar, N. C. Murmu, H. Koo and T. Kuila, *ACS Appl. Mater. Interfaces*, 2019, **11**, 21634–21644.

41 H. S. Jadhav, A. Roy, G. M. Thorat, W.-J. Chung and J. G. Seo, *J. Ind. Eng. Chem.*, 2019, **71**, 452–459.

42 Z. Yin, S. Zhang, J. Li, S. Ma, W. Chen, X. Ma, Y. Zhou, Z. Zhang and X. Wang, *New J. Chem.*, 2021, **45**, 12996–13003.

43 D. Kalpana and M. Ananth, *Trans. IMF*, 2005, **83**, 137–140.

44 M. Wang, L. Zhang, Y. He and H. Zhu, *J. Mater. Chem. A*, 2021, **9**, 5320–5363.

45 G. Zhao, K. Rui, S. X. Dou and W. Sun, *Adv. Funct. Mater.*, 2018, **28**, 1803291.

46 Q. Qu, J.-H. Zhang, J. Wang, Q.-Y. Li, C.-W. Xu and X. Lu, *Sci. Rep.*, 2017, **7**, 41542.

47 R. D. Nikam, A.-Y. Lu, P. A. Sonawane, U. R. Kumar, K. Yadav, L.-J. Li and Y.-T. Chen, *ACS Appl. Mater. Interfaces*, 2015, **7**, 23328–23335.

48 A. Fathollahi, T. Shahrabi and G. B. Darband, *J. Mater. Chem. A*, 2024, **12**, 9038–9054.

49 Y. Dong, S. Ji, H. Wang, V. Linkov and R. Wang, *Dalton Trans.*, 2022, **51**, 9681–9688.

50 S. Vesztergom, A. Dutta, M. Rahaman, K. Kiran, I. Zelocualtecatl Montiel and P. Broekmann, *ChemCatChem*, 2021, **13**, 1039–1058.

51 H. Yang, X. Hao, J. Tang, W. Jin, C. Liu, H. Hou, X. Ji and J. Hu, *Appl. Surf. Sci.*, 2019, **494**, 731–739.

52 N. Lotfi and G. B. Darband, *J. Electrochem. Soc.*, 2022, **169**, 096508.

53 S. Swathi, R. Yuvakkumar, P. S. Kumar, G. Ravi and D. Velauthapillai, *Fuel*, 2021, **303**, 121293.

54 C. Cheng, D. Kong, C. Wei, W. Du, J. Zhao, Y. Feng and Q. Duan, *Dalton Trans.*, 2017, **46**, 5406–5413.

55 S. Li, M. Li and Y. Ni, *Appl. Catal., B*, 2020, **268**, 118392.

56 X. Wu, C. Yong, X. An, Q. Kong, W. Yao, Y. Wang, Q. Wang, Y. Lei, W. Li and Z. Xiang, *New J. Chem.*, 2021, **45**, 18482–18490.

57 Z. Xu, Q. Chen, Q. Chen, P. Wang, J. Wang, C. Guo, X. Qiu, X. Han and J. Hao, *J. Mater. Chem. A*, 2022, **10**, 24137–24146.

58 Y. Jin, Q. Ke, D. Li, Z. Lei, Q. Ling, J. Xu and P. Cui, *ChemistrySelect*, 2018, **3**, 2812–2818.

59 B. Zhao, J. Liu, C. Xu, R. Feng, P. Sui, L. Wang, J. Zhang, J. L. Luo and X. Z. Fu, *Adv. Funct. Mater.*, 2021, **31**, 2008812.

60 S. Chu, W. Chen, G. Chen, J. Huang, R. Zhang, C. Song, X. Wang, C. Li and K. K. Ostrikov, *Appl. Catal., B*, 2019, **243**, 537–545.

61 X. Yang, J. Cheng, X. Yang, Y. Xu, W. Sun and J. Zhou, *Chem. Eng. J.*, 2022, **431**, 134171.

62 K. E. Salem, A. A. Saleh, G. E. Khedr, B. S. Shaheen and N. K. Allam, *Energy Environ. Mater.*, 2023, **6**, e12324.

63 L. Wei, L. Qiu, Y. Liu, J. Zhang, D. Yuan and L. Wang, *ACS Sustainable Chem. Eng.*, 2019, **7**, 14180–14188.

64 Y. Teng, X. D. Wang, J. F. Liao, W. G. Li, H. Y. Chen, Y. J. Dong and D. B. Kuang, *Adv. Funct. Mater.*, 2018, **28**, 1802463.

65 X. Cao, J. Wu, C. Jin, J. Tian, P. Strasser and R. Yang, *ACS Catal.*, 2015, **5**, 4890–4896.

66 J. Pan, P. Wang, P. Wang, Q. Yu, J. Wang, C. Song, Y. Zheng and C. Li, *Chem. Eng. J.*, 2021, **405**, 126622.

67 H.-C. Huang, Y.-C. Lin, S.-T. Chang, C.-C. Liu, K.-C. Wang, H.-P. Jhong, J.-F. Lee and C.-H. Wang, *J. Mater. Chem. A*, 2017, **5**, 19790–19799.

68 K. Hu, L. Tao, D. Liu, J. Huo and S. Wang, *ACS Appl. Mater. Interfaces*, 2016, **8**, 19379–19385.

69 M. Wang, L. Zhang, J. Pan, M. Huang and H. Zhu, *Nano Res.*, 2021, **14**, 4740–4747.

70 X. Li, W. Yan, S. Guo, Y. Liu, J. Niu, L. Yin and Z. Wang, *Electrochim. Acta*, 2021, **387**, 138488.

71 G. B. Darband, M. Aliofkhazraei, A. S. Rouhaghdam and M. Kiani, *Appl. Surf. Sci.*, 2019, **465**, 846–862.

72 S. Xu, X. Yu, X. Liu, C. Teng, Y. Du and Q. Wu, *J. Colloid Interface Sci.*, 2020, **577**, 379–387.

73 R. Abedi and G. Barati Darband, *Adv. Sustainable Syst.*, 2024, 2400465.

74 Y. Pan, X. Wang, H. Lin, Q. Xia, M. Jing, W. Yuan and C. Li, *Nanoscale*, 2023, **15**, 14068–14080.

75 X. Wang, J. Le, Y. Fei, R. Gao, M. Jing, W. Yuan and C. Li, *J. Mater. Chem. A*, 2022, **10**, 7694–7704.